An Improved Pattern Informatics Method for Extracting Ionospheric Disturbances Related to Seismicity Based on CSES Data: A Case Study of the *M*w 7.3 Maduo Earthquake

Weixi Tian[1], Yongxian Zhang[2]*, Changhui Ju[2], Shengfeng Zhang[2], Maoning Feng[2], Fengli Liu[3]

1 Institute of Geophysics, China Earthquake Administration, Beijing 100081, China
2 Institute of Earthquake Forecasting, China Earthquake Administration, Beijing 100036, China
3 Department of Earth and Space Sciences, Southern University of Science and Technology, Shenzhen 518055, China

* Corresponding author, Email: yxzhseis@sina.com

Key Points:

- Proposed an Improved Pattern Informatics Method for processing electron density data and capturing anomalous spatio-temporal pattern
- Conducted a feasibility study of the method using the 2021 Maduo *M*w7.3 Earthquake as a case study
- Observed a recurring emergence and dissipation in the electron density prior to the Maduo *M*w7.3 Earthquake

Abstract: The exploration of multi-layer coupling mechanisms between earthquakes and the ionosphere is crucial for utilizing ionospheric precursors in earthquake prediction. A significant research task involves continuously tracking the spatio-temporal changes in ionospheric parameters, acquiring comprehensive seismic anomaly information, and capturing "deterministic" precursor anomalies. Building upon previous research on seismic ionospheric signal characteristics and data from the China Seismo-Electromagnetic Satellite (CSES), we have enhanced the Pattern Informatics(PI) Method and proposed an Improved Pattern Informatics(IPI) Method. The IPI method enables the

calculation of the spatio-temporal dynamics of electronic density anomalies detected by the CSES satellite. Taking the 2021 Maduo *M*w7.3 earthquake as a case study, we analyzed the seismic signals potentially contained in the electronic density anomaly disturbances. The results show that: 1) Compared to original electronic density images, the IPI method-derived models extracted distinct electronic density anomaly signals, regardless of the data collected whether during descending (daytime) or ascending (nighttime) orbits, or across different time scales of change window. 2) The electronic density anomalies appeared about 40 days prior to the Maduo *M*w7.3 earthquake. The evolution of these anomalies followed a pattern of appearance, persistence, disappearance, re-emergence, and final disappearance. Moreover, the evolution trends of the IPI hotspot images calculated from descending and ascending orbit data were similar. These results suggest that the IPI method can capture the spatio-temporal trends of ionospheric parameters and effectively extract electronic precursors related to strong earthquakes.

Keywords：Improved Pattern Informatics Method(IPI Method)；China Seismo-Electromagnetic Satellite(CSES)；Seismo-Ionospheric Disturbances; *M*w 7.3 Maduo Earthquake; Earthquake Prediction.

1. Introduction

Since Gokhberg(1982) first detected pre-seismic electromagnetic signal anomalies in satellite data, several countries have incorporated electromagnetic satellite monitoring into their space development programs. These include Russia's Predvestnik-E, COMPASS-I, and II satellites, the United States' QUAKESAT, and France's DEMETER satellite. Electromagnetic satellite monitoring offers advantages over terrestrial geophysical monitoring methods due to its global reach, short periods, high efficiency, dynamism, and all-weather capabilities (Zhuo Xianjun *et al*., 2005). The potential applications of this technology in earthquake mechanism research and seismic monitoring and prediction have made the study of pre-seismic electromagnetic anomalies using satellite data a new research hotspot (Zhang *et al*., 2023). Following the launch of the China Seismo-Electromagnetic Satellite (CSES)

on February 2, 2018, a series of studies have been conducted in various areas. These include data availability (Yan *et al.*, 2020; Liu *et al*., 2021), global geomagnetic models (Yang *et al*., 2021), ionospheric events such as magnetic storms (Spogli *et al*., 2021), statistical characteristics of seismic ionospheric disturbances (Li *et al*., 2020; De Santis *et al*., 2021), and multi-layer coupling (Marchetti *et al*., 2019; Zhao *et al*., 2021; Liu *et al*., 2023; Zhang *et al*., 2023).

During the operational period of the CSES satellite, more than 500 earthquakes of magnitude 6 and above, and nearly 60 of magnitude 7 and above, occurred globally (Shen *et al*., 2023). This provided a rich data source for studying the correlation between ionospheric observations and earthquakes. Many scholars have attempted to extract ionospheric disturbances and precursory information related to earthquakes from the vast amount of CSES satellite data (Marchetti *et al*., 2019; Li *et al*., 2020; Yang *et al*., 2021; De Santis *et al*., 2021). Statistical studies have shown a clear spatio-temporal correlation between earthquakes and electron density anomalies (Li *et al*., 2020, 2023; De Santis *et al*., 2019; Liu *et al*., 2022). Although current research has gained an initial understanding of the spatio-temporal characteristics of seismic ionospheric precursor information, previous anomaly extraction methods, such as sliding principal component analysis (PCA) method (Chang *et al*., 2017), Wavelet and Bispectral techniques (Sondhiya *et al*., 2014), and quartile methods (Zhang *et al*., 2020), mostly use data from single or partial orbits, making it challenging to simultaneously capture anomalies in the epicenter and surrounding areas (Zheng *et al*., 2023). Moreover, the lower spatial resolution and discontinuous measurements of satellite observations hinder the continuous tracking of seismic-ionospheric signal changes, impacting our understanding of the temporal and spatial evolution of these signals (Zhang *et al*., 2023). Therefore, to capture ionospheric anomalies reflecting the seismic incubation process, detect precursory anomalies related to earthquakes, and explore the multi-layer coupling mechanism between earthquakes and the ionosphere, further development and research into methods for extracting ionospheric disturbance anomalies are still needed.

Rundle et al. (2000, 2002) developed the PI method for studying earthquake activity, which has shown promising predictive performance in medium-long-term

earthquake forecasting. Wu et al. (2011) made modifications to the PI algorithm, proposing the Modified Pattern Informatics (MPI) method, which was successfully applied to the analysis of DEMETER satellite data anomalies, providing images of the ionospheric anomaly evolution before the Wenchuan earthquake and confirming the feasibility of applying the MPI method to electromagnetic satellite observation data processing. The MPI method, through grid-based and interpolation data processing techniques, overcomes the discontinuity and low spatial resolution issues of satellite observations. However, it has not yet considered specific data characteristics such as the orbital altitude of CSES (Liu *et al*., 2021), nor propagation features of seismic-ionospheric signals including the range of earthquake anomaly (De Santis *et al*., 2019) and negative ionospheric anomalies associated with earthquakes (Akhoondzadeh *et al*., 2010).

In this study, we take into account the electron density data characteristics of the CSES satellite and the features of seismic-ionospheric signals to enhance the PI method, introducing an Improved Pattern Informatics (IPI) method. We evaluate the efficacy and reliability of this method by examining the case of the 2021 *M*w7.3 Maduo earthquake in Qinghai. Through the analysis of continuous spatio-temporal evolution images of the IPI hotspots, we identify potential ionospheric anomaly signals that emerged before and after the earthquake.

2.Data

2.1. Ionospheric Data Recorded by CSES

The China Seismo-Electromagnetic Satellite (CSES), also known as Zhangheng-1 Electromagnetic Satellite (ZH-01), is the first microsatellite for monitoring seismic electromagnetic activities (Shen *et al*., 2018). It operates in a circular sun-synchronous orbit at an altitude of 507 kilometers, with its descending node aligning with 14:00 local time (LT) and a revisit period of 5 days. The satellite's operational region spans the latitude range of [−65°, 65°]. Equipped with eight payloads, including a Langmuir probe that primarily measures electron temperature and density with a one-second temporal resolution (Liu *et al*., 2019), this study employs electron density data captured by the CSES Langmuir probe from January 1, 2019, to December 31, 2021.

2.2. Data Process

The IPI method's enhanced spatio-temporal integration capability is derived from the spatial and temporal grid division of the data. Therefore, preprocessing of the CSES data is necessary to create an "Ionospheric Parameter Catalog" containing time, longitude, latitude, and observational values. The specific steps are as follows:

Grid Division: Based on the grid correlation of ionospheric parameters (Yao *et al*., 2014) and the orbital characteristics of the CSES satellite, the operational range of the CSES orbit is divided into grids of 5°× 2° (longitude× latitude).

Moore Neighbor Interpolation: After grid division, it's essential to calculate the mean value of ionospheric parameters for each grid and assign it to the grid's center point. To obtain the daily two-dimensional distribution of ionospheric parameters in the CSES monitoring area and mitigate the issue of large gaps between adjacent orbits and sparse data in the longitude direction, grids without data utilize the Moore Neighboring principle (Chen *et al*., 2005). This involves averaging the parameters from the eight neighboring grids surrounding the $N(x_i, y_j)$ grid and assigning this average to the $N(x_i, y_j)$ grid as the ionospheric parameter for that day, as illustrated in Figure 1.

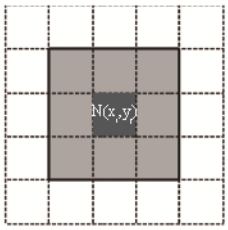

Figure 1 Moore neighbor interpolation

Establishing an Annual Model of Ionospheric Parameters: Due to issues such as instrument malfunctions, some grids still have discontinuous data sequences. Therefore, we construct a time series for the ionospheric parameters of each grid. Using cubic spline interpolation, we interpolate these time series to create an annual model for the ionospheric parameters of all grid points.

Developing a Dynamic Ionospheric Background Field: Considering the annual and seasonal variations, long-term trends of the ionosphere, and factors like the Equatorial Ionization Anomaly (EIA), Weddell Sea Anomaly (WSA), and other

large-scale ionospheric structures (Li *et al*., 2023), we establish a daily dynamic background field for the ionosphere, as illustrated in Figure 2. The original observational data and the residual values from the background field are used as input for the IPI method. After removing the dynamic background field of the ionospheric parameters, we obtain an "Ionospheric Parameter Catalog" containing date, latitude, longitude, and residual values.

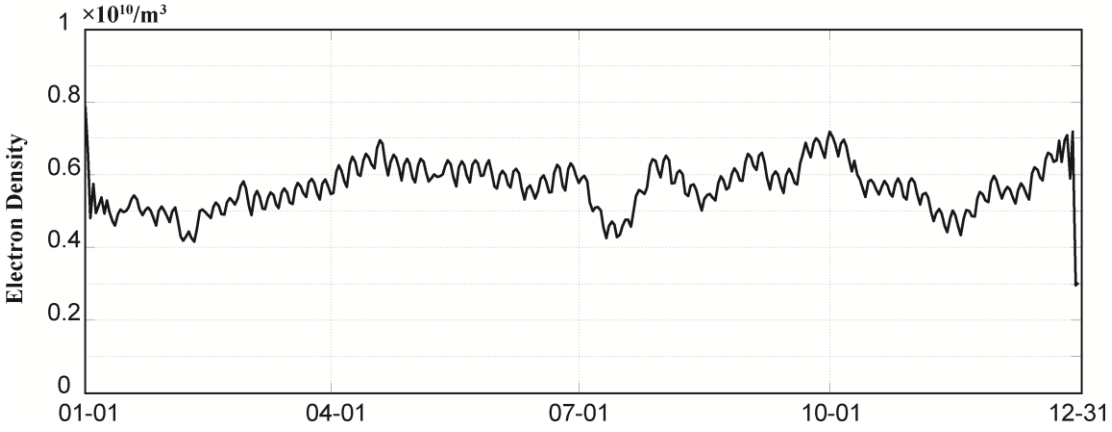

Figure 2 Dynamic background field

The grid (97.5°E, 30°N) is used as an example.

3. Method

3.1. Pattern Informatics Method

PI divides a region into N grids and defines an N-dimensional system state vector built on Hilbert space (consisting of a time series of seismic times from the N grids). It considers this system state vector to represent the seismicity of a region and its value to be a constant. The phase angle of this system vector varies with time. If the relative rate of seismic activity intensity of a unit vector varies too much, its phase angle will undergo a continuous rotation away from the quantifiable average value, which is known as the drift of the phase angle. According to PI, the change in the activity pattern of small earthquakes is represented by the drift of the phase angle (Rundle *et al*., 2000, 2002).

The process entailed dividing the study area into spatial and temporal grids, constructing a frequency time series of the seismic events larger than a certain magnitude threshold in each grid, normalizing the intensity of seismic events, calculating the deviation of the intensity function from the background in each grid

and calculating the probability of seismic events. The probability of seismic events in each grid was then normalized to the probability of occurrence and the grid with a high probability of seismic events was detected after deducting the background probability, i.e., "seismic hotspots"(Chen *et al*., 2005).

3.2. Improved Pattern Informatics Method (IPI)

We refined the PI method to develop the IPI method, based on the characteristics of seismic-ionospheric signals and the features of CSES data. Key improvements include defining the study area, modifying the method for calculating anomalies, eliminating the spatial application of Moore's principle and the forecasting period, and computing negative ionospheric anomalies. The specific process of the IPI method is as follows:

(1) The study area is determined using the empirical formula for the seismogenic zone range (Dobrovolsky *et al*., 1979), as shown in Equation （2.1）.

$$R = 10^{0.43M}$$

$$R_{OPI} = \sqrt{2}R \qquad (2.1)$$

Where M is the magnitude, and R is the radius of the seismogenic zone. Considering the data preprocessing process where data is divided into rectangular grids, and to ensure that the study area is within the Dobrovolsky seismogenic zone range, we set the Dobrovolsky seismogenic zone as the circumscribed circle of the study area, with R_{OPI} being the side length of the square. For instance, for a *M*7.0 earthquake, the radius *R* of the seismogenic zone is approximately 1023 km, and the side length of the study area's square is about 1447 km.

(2) Grid Division: The IPI method allows for the selection of different grid sizes based on the spatial resolution of the data. However, the preprocessing, based on the findings of Yao et al. (2014) and the orbital characteristics of the CSES satellite, results in an "Ionospheric Parameter Catalog" with a precision of 5°×2°. Consequently, the grid division for the IPI study area also adopts this size of 5°×2°.

(3) Setting a Lower Threshold N_C, and identifying anomalies using a Boolean function(Tiampo *et al*., 2002): Each grid constructs a time series $N_i(\mathrm{t})$,

representing the number of times the residual value in a given grid exceeds the lower threshold N_C within a unit of time. In constructing $N_i(\mathrm{t})$, the spatial Moore's principle is omitted. This is because, in seismological PI methods, Moore's principle is applied to account for earthquake location errors, which is not applicable to ionospheric data. The use of a Boolean function and the lower threshold N_C categorizes values above N_C as 1 and below N_C as 0, assigning equal weight to anomalies of varying magnitudes. This approach, in contrast to differential calculations of absolute anomaly values (Wu *et al.*, 2011), mitigates the impact of extreme value anomalies on the results, enhancing the stability of anomaly detection.

(4) Defining Five Time Points and Two Time Windows: The time points are designated as t_0、t_b、t_1、t_2, and an arbitrary time t, illustrated in Figure 3. We have omitted the predictive period $t_2 \sim t_3$ (Rundle *et al.*, 2000, 2002) from our analysis. This is based on the fact that the original PI algorithm's predictive period is founded on the average field properties of dynamic diffusion, and whether ionospheric parameter variations conform to this property requires further investigation.

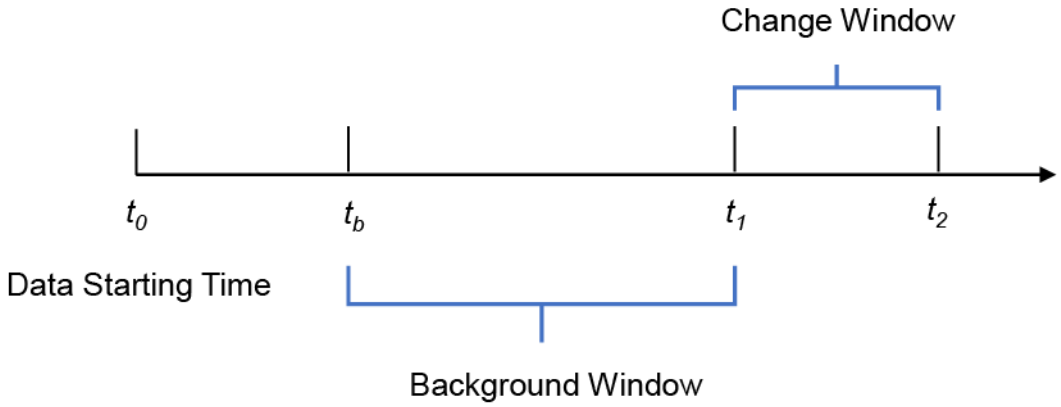

Figure 3 Time window division

t_0 is the start time of the data, the background time window is from t_b to t_1 ($t_0 \le t_b \le t_1$), and the change time window is from t_1 to t_2.

Considering that a longer background window can contain more information, but the variation of ionospheric parameters is rapid, an excessively long background window might include irrelevant information in the calculation. Therefore, this study selected a background window of 6 months. The selection of the change

window will be thoroughly described in Section 4.

(5) Define the ionospheric parameter intensity function as $I_i(t_b, t)$, and calculate the average number of instances where the grid i exceeds the minimum ionospheric parameter threshold N_C from t_b to t.

$$I_i(t_b, t) = \frac{1}{t-t_b}\sum_{t'=t_b}^{t} N_i(t') \quad (2.2)$$

(6) By calculating the difference between the ionospheric parameter during the change window and the background window, we obtain the ionospheric parameter anomaly intensity function $\Delta I_i(t_b, t_1, t_2)$.

$$\Delta I_i(t_b, t_1, t_2) = I_i(t_b, t_2) - I_i(t_b, t_1) \quad (2.3)$$

(7) In order to obtain the relative ionospheric parameter anomaly intensity function for each grid in the research area, normalize the ionospheric parameter anomaly intensity function.

$$\Delta\widehat{I}_i(t_b, t_1, t_2) = \frac{\Delta I_i(t_b,t_1,t_2) - \langle \Delta I_i(t_b,t_1,t_2)\rangle}{\sigma(t_b,t_1,t_2)} \quad (2.4)$$

Where $\langle \Delta I_i(t_b, t_1, t_2)\rangle$is the average ionospheric parameter anomaly intensity function for all grids, and $\sigma(t_b, t_1, t_2)$is the standard deviation of the ionospheric parameter anomaly intensity function for all grids.

(8) To eliminate the "noise" associated with extremely small change, we calculate the average change of the normalized background anomaly ionospheric parameter according to equation (2.4).

$$\overline{\Delta\widehat{I}_i(t_b, t_1, t_2)} = \frac{1}{t_1-t_0}\sum_{t_b=t_0}^{t_1} \Delta\widehat{I}_i(t_b, t_1, t_2) \quad (2.5)$$

(9) Define the probability of an anomalous disturbance occurring in grid i as $P_i(t_0, t_1, t_2)$, which is the exponential function of the absolute average change of the normalized ionospheric parameter anomaly intensity function.

$$P_i(t_0, t_1, t_2) = e^{|\Delta I_i(t_0,t_1,t_2)|} \quad (2.6)$$

(10) The original PI did not take into account the negative ionospheric anomalies associated with earthquakes (Akhoondzadeh *et al*., 2010; Liu *et al*., 2022). Therefore, we have modified the formula from $P_i(t_0, t_1, t_2) = e^{\Delta I_i(t_0,t_1,t_2)}$ (Wu

et al., 2011) to $P_i(t_0, t_1, t_2) = e^{|\Delta I_i(t_0,t_1,t_2)|}$,ensuring the IPI calculation can capture both positive and negative ionospheric anomalies.

(11) We calculate the average probability of anomalous disturbances occurring in all grids in the research area as the background probability. The relative change is then obtained by subtracting the background probability from the individual grid probabilities.

$$\Delta P_i(t_0, t_1, t_2) = P_i(t_0, t_1, t_2) - \langle P_i(t_0, t_1, t_2) \rangle \quad (2.7)$$

For grids with positive values, i.e., grids where $P_i(t_0, t_1, t_2) > 0$, we designate them as hotspots (anomalous areas).

(12) To better analyze the evolution process of seismic ionospheric signals and highlight anomalies, we can slide t_0, t_1, t_2, and t_3 with a fixed sliding step size to obtain continuous results over multiple days. Finally, we can normalize all the results to obtain the Standard IPI hotspots (SIPI).

$$S_{IPI} = \frac{\Delta P_i(t_0,t_1,t_2)}{\Delta P_i(t_0,t_1,t_2)_{max}} \quad (2.8)$$

4. IPI method in the identification of spatio-temporal ionospheric anomalies before the Maduo *M*w7.3 earthquake

On May 22, 2021, a *M*w7.3 earthquake occurred in Maduo County, Qinghai Province, China (34.598°N, 98.251°E), with a focal depth of 10km. Based on the IPI method and using electron density data observed by the CSES satellite, we constructed multiple models to calculate the pre- and post-earthquake electron density anomalies in Maduo. Additionally, we analyzed the spatiotemporal dynamics of electron density using IPI hotspot maps.

Due to the significant increase in ionospheric electron density caused by solar radiation during the day, nighttime data is generally used for extracting ionospheric anomalies (Guo *et al*., 2022; Wen *et al*., 2022). The IPI algorithm is adaptive, capable of effectively eliminating background trends and noise, and theoretically can mitigate the influence of daytime solar activities. Therefore, we processed both ascending and descending orbit data separately, computing their respective original electron density

images and IPI hotspot maps. This approach allowed a more comprehensive study of the spatiotemporal characteristics of electron density before the earthquake and explored the potential of this method for extracting anomalies from daytime ionospheric data.

4.1. Spatio-temporal images with electron density

To dynamically track the detailed characteristics of the original electron density evolution over time, ensuring data readability and consistent measurement properties, we obtained normalized spatio-temporal images of electron density for 90 days before and 7 days after the Maduo *M*w7.3 earthquake, as shown in Figure 4. The study area was determined based on formula (2.3), with an R_{OPI} of approximately 1000Km. The spatial extent of the study area is marked in Figure 4, which is consistent with the subsequent IPI study region.

Figure 4 (A) and (B) represent the results from descending (daytime) and ascending (nighttime) data, respectively. The results indicate no significant abnormal disturbances in the original electron density observations before and after the Maduo *M*w7.3 earthquake, rendering it impossible to derive meaningful seismic ionospheric disturbance information.

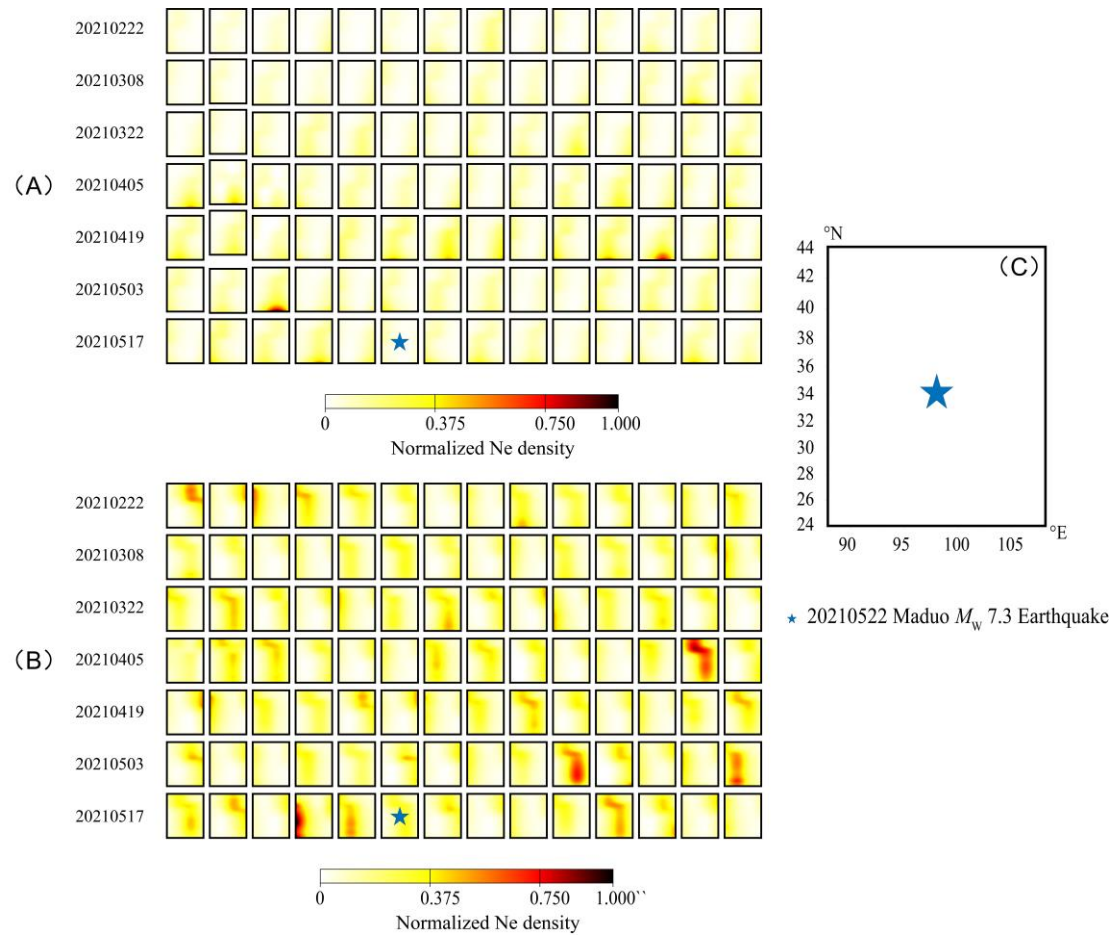

Figure 4 Normalized electron density spatio-temporal images

(A) Descending (daytime) electron density data spatio-temporal image; (B) Ascending (nighttime) electron density data spatio-temporal image; (C) The spatio-temporal range of the study area, same below.

4.2. Spatial and Temporal IPI Hotspots images before and after *M*w7.3 Maduo earthquake

Seismological PI research indicates that the change window on different scales significantly affects the predictive efficacy of the PI method (Zhang *et al*., 2017), To verify the effectiveness of the IPI method in extracting seismic ionospheric precursor information, we constructed models on various temporal scales and calculated to obtain IPI hotspot images for 90 days before and 7 days after the earthquake, as shown in Figures 5 and 6.

In Figures 5 and 6, the change windows (A) - (D) are set to 5, 10, 15, and 20 days respectively. The red pentagram marks the date of the Maduo earthquake. Based on this, we analyzed the IPI hotspot features of models constructed with different

change windows, as seen in Table 1.

Table 1 IPI hotspot features of models with different scale change windows

Change Window	5d	10d	15d	20d
IPI Hotspots features	IPI hotspots emerge before the earthquake, but their spatio-temporal distribution is disordered and chaotic	Continuous IPI hotspots appear before the earthquake and weaken before earthquake	Continuous IPI hotspots emerge before the earthquake and persist for a period after the earthquake	Continuous IPI hotspots appear after the earthquake

Based on the analysis of Figure 5, 6 and Table 1, We find:

(1) The IPI method can extracts ionospheric anomalies from descending orbit (daytime) data.

(2) Models constructed with different scale change windows can capture ionospheric disturbances. However, there are differences in the disturbances detected by each model. The IPI model with a change window of t_2-t_1=10 days yields better results in capturing anomalies before and after the earthquake.

(3) Models constructed with different scale change windows can capture ionospheric disturbances. However, there are differences in the disturbances detected by each model. The IPI model with a change window of t_2-t_1=10 days yields better results in capturing anomalies before and after the earthquake.

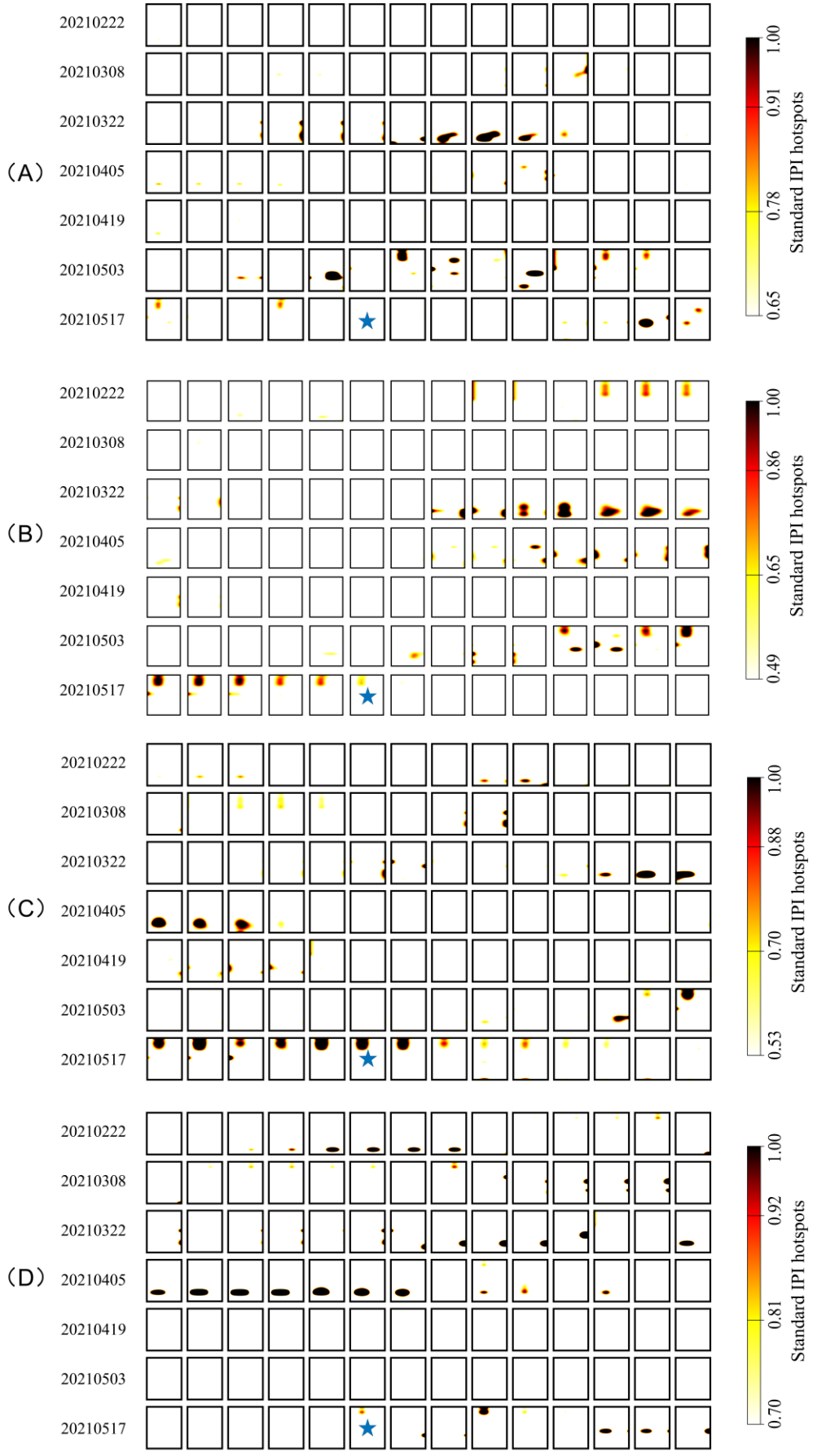
(A)
(B)
(C)
(D)
20210222
20210308
20210322
20210405
20210419
20210503
20210517
Standard IPI hotspots
1.00
0.91
0.78
0.65
0.86
0.49
0.88
0.53
0.92
0.81
0.70
★ 20210522 Maduo M_W 7.3 Earthquake

Figure 5 IPI hotspots image based on descending orbit data

(A) t_2-t_1=5d. (B) t_2-t_1=10d. (C) t_2-t_1=15d. (D) t_2-t_1=20d. The date on the left corresponds to the first image of each row, with the research area being the same as that in Figure 4.

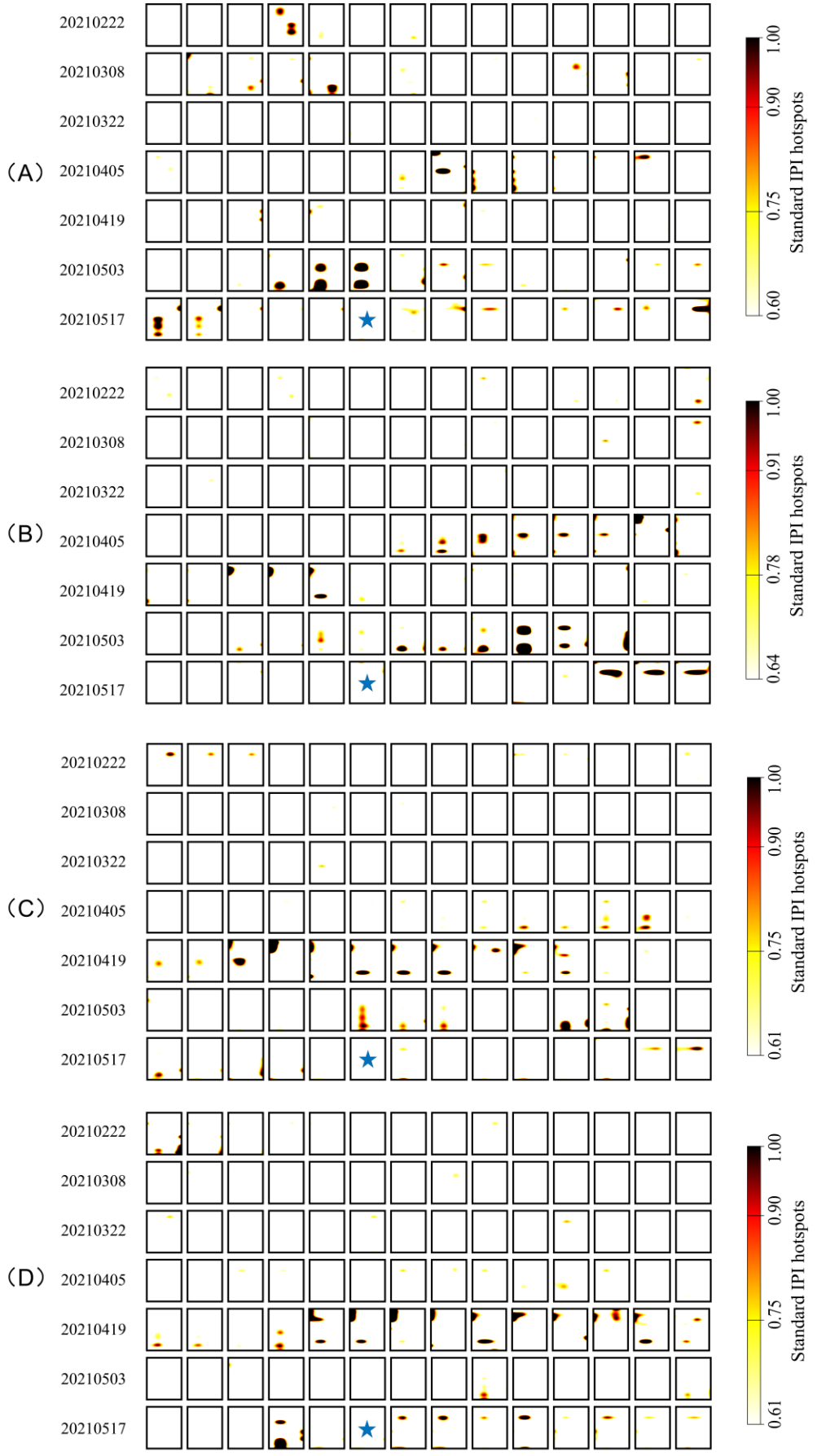
(A)
(B)
(C)
(D)
20210222
20210308
20210322
20210405
20210419
20210503
20210517
Standard IPI hotspots
1.00
0.90
0.75
0.60
0.91
0.78
0.64
0.61
★ 20210522 Maduo M_W 7.3 Earthquake

Figure 6 IPI hotspots image based on ascending orbit data

(A) t_2-t_1=5d. (B) t_2-t_1=10d. (C) t_2-t_1=15d. (D) t_2-t_1=20d. The date on the left corresponds to the first image of each row, with the research area being the same as that in Figure 4.

5. Discussion

Based on the spatio-temporal evolution characteristics of CSES electromagnetic satellite observation data and earthquake-ionospheric precursor features, we optimize the PI method to develop the IPI method. Using the 2021 Maduo *M*w7.3 earthquake as a test case for the method's effectiveness and reliability, the results indicate that: 1) The IPI can extract ionospheric anomaly information from descending (daytime) data. 2) Models constructed for different scale change windows can capture ionospheric disturbances, though the disturbances detected by each model differ, with the IPI model for a change window of t_2-t_1=10 days obtaining better pre- and post-earthquake anomaly information. 3) The IPI hotspot maps calculated from descending (daytime) and ascending (nighttime) data show similarities in trends and differences in spatio-temporal locations.

The results of the Maduo *M*w7.3 earthquake demonstrate that the IPI method can extract significant ionospheric disturbance signals. Previous research has shown a significant statistical correlation between shallow earthquakes with magnitudes M≥5.5 and variations in the ionospheric anomalies (De Samtis *et al*., 2019, 2021; Yan *et al*., 2017). The ionosphere is also influenced by multiple factors, such as solar activity, geomagnetic storms, and geomagnetic activities (Du *et al*., 2022), and it remains unknown whether the anomalies present in Figures 5 and 6 are caused by the Maduo *M*w7.3 earthquake. To comprehensively analyze factors related to IPI hotspots, we will utilize earthquakes within the study area with *M*w≥5.5, the Kp index indicating geomagnetic activity strength, the Dst index reflecting the intensity of geomagnetic storms, and the F10.7 index denoting solar activity (collectively referred to as space weather indices) for the analysis of IPI model hotspots in a change window of t_2-t_1=10 days (Fejer *et al*., 1991; Liu *et al*., 2022).

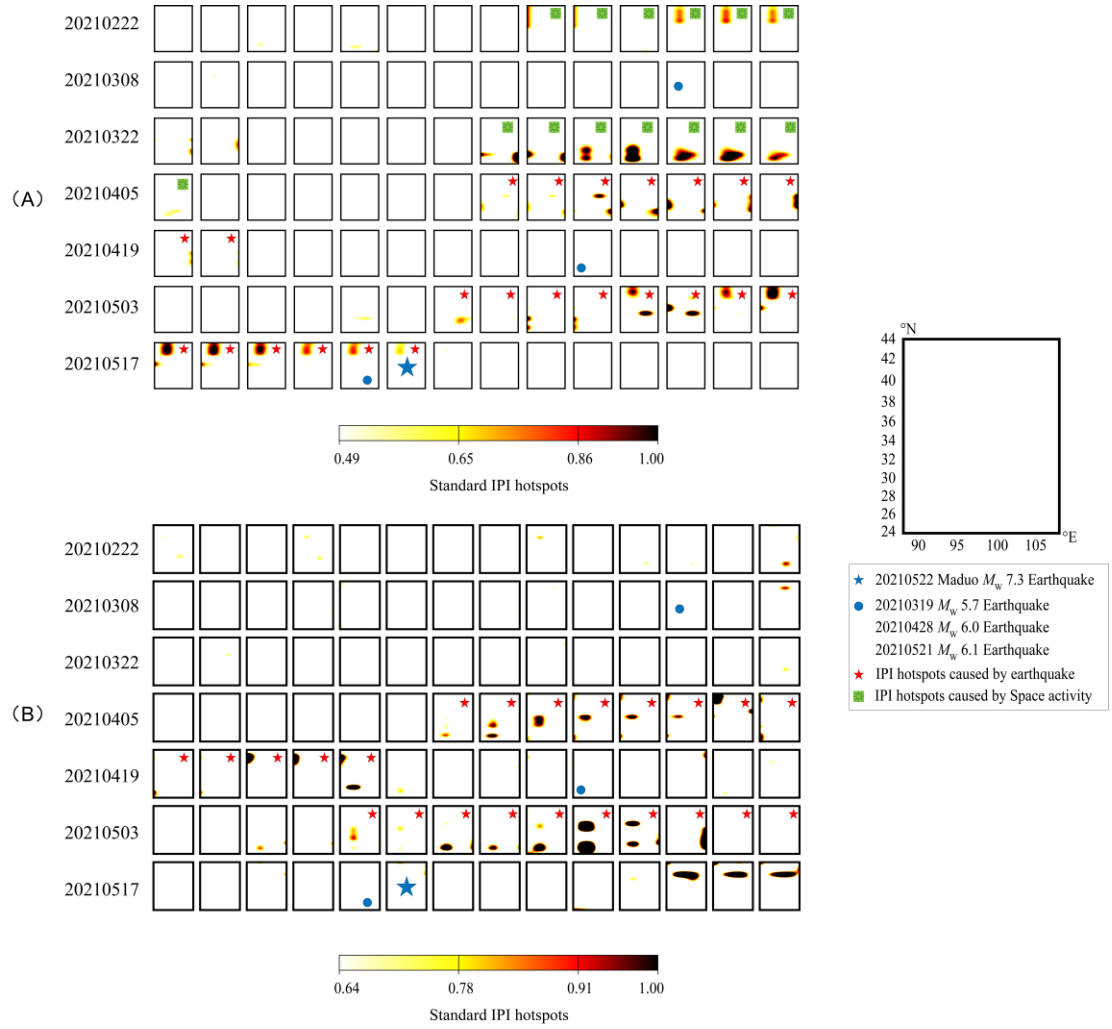

Figure 7 IPI hotspots image for t_2-t_1=10d

(A)Results of descending (daytime) data. (B) Results of ascending (nighttime) data. The date on the left corresponds to the first image in each row. The blue pentagram represents the epicenter of the Maduo *M*w7.3 earthquake, and the blue circles mark earthquakes within the study area with magnitudes ≥*M*w5.5. The IPI hotspot periods are divided into: March 2-7 (Period 1), March 29-April 5 (Period 2), April 12-20 (Period 3), May 9-23 (Period 4), April 11-24 (Period 5), and May 5-14 (Period 6). The red pentagrams indicate that the IPI hotspots in these periods are caused by earthquakes, and the green suns indicate that they are caused by space weather activities.

Within the spatio-temporal scope of the IPI study, three earthquakes with *M*w≥5.5 occurred: the March 19, 2021 Naqu, Xizang *M*w5.7 earthquake in China (31.925°N, 92.915°E), the April 28 Dhekiajuli *M*w6.0 earthquake in India(26.781°N, 92.457°E), and the May 21 *M*w6.1 Yangbi, Yunnan earthquake in China(25.727°N, 100.008°E). Based on the general empirical laws proposed by Rikitake (1987) and the seismogenic zone empirical formula by Dobrovolsky (1979), the anomalous periods for *M*w=5.5 and *M*w=6.1 earthquakes occurred approximately 16 and 26 days before

the earthquakes, respectively, mainly within a 400 km range. We will analyze the earthquake-IPI hotspots based on the aforementioned conditions.

The IPI method uses Boolean functions and a threshold N_C to determine anomalies, calculating the relative changes between the change window (t_1-t_2) and the background window (t_b-t_1), with the resulting anomaly values assigned to t_2. This means that the anomaly value at t_2 depends on the frequency of electron density disturbances above N_C during the change window. If activities such as solar, geomagnetic, and magnetic storms occur within the change window and cause electron density disturbances greater than the threshold N_C, they will affect the IPI results, but the extent of the impact depends on the duration of these activities, i.e., the frequency of anomalies. Previous studies indicate that a Kp index over 3 suggests high geomagnetic activity, a Dst index greater than -30nT signals a geomagnetic storm, and an F10.7 index above 100 denotes solar activity (Li *et al*., 2022). Assuming that these geomagnetic and solar activities cause disturbances in electron density, which exceed the threshold N_C only on the same day. We established that only when more than 50% of the change interval exhibits the aforementioned activities is an IPI hotspot attributed to geomagnetic, solar, or storm activities, termed $W_{\mathrm{IPI.}}$ Hence, we computed the space weather indices for the entire study duration of the Maduo *M*w7.3 earthquake to locate intervals likely to produce W_{IPI}, as depicted in Figure 8.

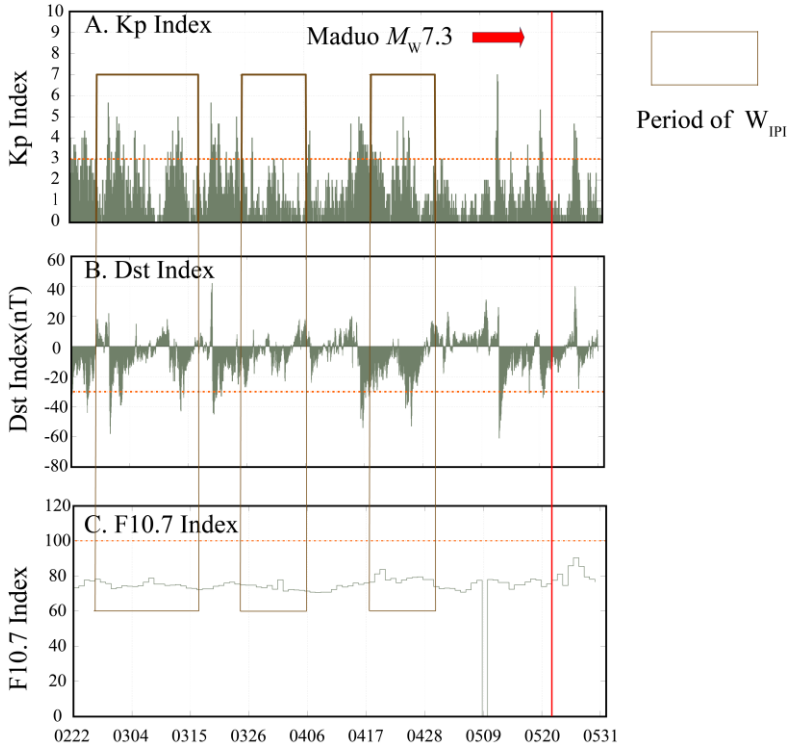

Figure 8 Space weather incidex image

(A) a bar chart of the Kp index. (B) a bar chart of the Dst index. (C) a step chart of the F10.7 index. Each index's threshold marked by an orange dashed line, and periods meeting the WIPI criteria highlighted with brown rectangles

According to the results in Figure 7 (A), the main IPI hotspots were concentrated in four periods in 2021: March 2-7 (Period 1), March 29 to April 5 (Period 2), April 12-20 (Period 3), and May 9-23 (Period 4). Figure 7 (B) shows that IPI hotspots were primarily distributed during two periods in 2021: April 11-24 (Period 5) and May 5-14 (Period 6). Based on the space weather index data in Figure 8, we calculated the primary periods for W_{IPI} to be February 27-28, March 1-17, March 26 - April 6, and April 19-30, 2021.

We analyzed the reasons for the IPI hotspot anomalies in each period, considering the intervals of W_{IPI} caused by space weather index anomalies and the spatial-temporal locations of earthquakes with *M*w≥5.5. Before the emergence of hotspots in the northern part of the study area from March 2-7, 2021 (Period 1) and the southwestern part from March 29-April 5, 2021 (Period 2) in Figure 7 (A), there were multiple occurrences of geomagnetic activity and storms. The periods of February 27-28, March 1-17, and March 26-April 6, 2021, were identified as the main intervals for W*IPI*, suggesting that the aforementioned hotspots might be related to

geomagnetic activities, among others. The hotspots in the eastern and western parts of the study area from April 12-20 (Period 3) and above and southwest of the epicenter from April 11-24 (Period 5) in Figure 7 (A) and (b) appeared before the W_{IPI} (April 19-30). Although there is some overlap between Periods 3 and 5 and this W_{IPI}, the primary time frames of Periods 3 and 5 precede the W_{IPI}. Moreover, after the occurrence of this W_{IPI}, the spatio-temporal trends of the hotspots in Periods 3 and 5 remained unchanged, unaffected by space weather. This indicates that the IPI hotspots during these periods are not related to solar activities, geomagnetic disturbances, or magnetic storms. They are likely related to crustal activities during the gestation of the April 28, 2021, *M*w6.0 earthquake and the Qinghai Maduo *M*w7.3 earthquake. Similarly, in Figure 7 (A), for May 9-23, 2021 (Period 4), the central and northern hotspots, and in Figure 7 (B), for May 5-14, 2021 (Period 6), the western and southwestern hotspots showed no significant geomagnetic storms or activity before their formation. Within 26 days following the anomalies, Yangbi *M*w6.1 and Maduo *M*w7.3 earthquake occurred within 400 km of the IPI hotspots, suggesting a possible connection with the seismic preparation phase of these earthquakes. Others' research on ionospheric anomalies associated with the Maduo earthquake revealed that anomalies were detected in the Dobrovolsky seismogenic zone as early as April 10, 2021, with intensification beginning about 20 days before the earthquake (Du *et al*., 2022) and significant increases in electron density observed approximately 14 days prior (Dong *et al*., 2022; Li *et al*., 2022).

We also observed that the evolution of IPI hotspots prior to the Maduo earthquake follows a pattern of appearance, persistence, disappearance, re-appearance, and re-disappearance. Previous models of lithospheric coupling, involving radon gas release due to rock layer activity, earth degassing caused by fluid migration, and the release of p-holes (positive holes), suggest that this trend is likely due to physicochemical changes in the lithosphere during the earthquake's gestation process (Hayakawa *et al*., 2004; Pulinets *et al*., 2011; Parrot *et al*., 2021). Similar ionospheric anomaly processes have also been observed in multi-layered coupling studies of the 2013 Lushan *M*w6.7 earthquake and the 2018 Indonesian *M*w7.5 earthquake (Marchetti *et al*., 2020; Zhang *et al*., 2022). Statistical studies based on SWARM

satellite electron density and magnetic field data revealed that anomalies before *M*w≥5.5 earthquakes are not limited to a specific time frame but occur in multiple intervals. This supports the theory that the recurring anomalies detected in our IPI hotspots might result from multi-layered coupling during the earthquake preparation phase. However, there is currently no mature theoretical model or mechanism for how earthquakes affect the ionosphere. The reasons why IPI hotspots exhibit such distinctive earthquake-ionosphere disturbance signals remain to be further explored in multi-layered coupling research.

IPI hotspots shows anomalies from around 40 days to approximately 15 days before earthquakes, extracting their spatio-temporal evolution process. This demonstrates the feasibility and effectiveness of this method in extracting seismic ionospheric anomaly data. This primarily relies on the adaptive nature of the IPI algorithm, which can mitigate the effects of background changes and noise to a certain extent. While the IPI method can capture the continuous spatio-temporal changes in ionospheric parameter anomalies, it still has many limitations in practical earthquake forecasting:

1) The space environment is influenced by various factors. The IPI method can only extract anomalies in ionospheric parameters but cannot directly filter out ionospheric precursor information caused by earthquakes. It is challenging to determine which earthquake caused the ionospheric anomalies in regions with multiple significant earthquakes. Establishing anomaly determination indicators and combining them with space weather indices like Kp and Dst for anomaly filtering could be an effective solution.

2) We use R from Dobrovolsky empirical formula, $R = 10^{0.43M}$, as the radius of the circumscribed circle of the rectangular study area to ensure it falls within the seismogenic zone. However, considering that magnetic field lines are not perpendicular to the ground and phenomena such as E×B drift and plasma diffusion occur during signal propagation (Liu *et al*., 2021), it is possible for earthquake ionospheric anomalies to appear outside the seismogenic zone. This understanding, also noted by Marchetti et al. (2020). Suggests that future research areas might need to be adjusted accordingly.

3) The study separately utilized descending (daytime) and ascending (nighttime) orbit data and designed periods of change window across different time scales for method testing. Although different IP models were able to extract distinct ionospheric anomaly disturbance signals, there were differences in the spatio-temporal distribution of these anomalies. This indicates that data selection and parameter setting greatly influence the final results of the IPI method. The setting of optimal parameters and the selection of data require further research.

6. Conclusion

Based on the PI method, we optimized the data processing by combining features of satellite observations and earthquake-ionospheric precursor characteristics, leading to the establishment of the IPI method. The method's reliability and effectiveness were validated using the 2021 *M*w7.3 Maduo earthquake in Qinghai, China, as a case study. The IPI calculation provided continuous spatio-temporal images of electron density anomalies, and potential earthquake-ionosphere anomaly disturbance signals were analyzed based on space weather indices and IPI hotspots.

The main research findings are as follows:

1) Based on CSES electron density data, the model constructed by the IPI method was able to extract electron density anomaly disturbance signals not presenting in normalized electron density spatio-temporal images, in both descending (daytime) and ascending (nighttime) orbits, and across various scales of change window.

2) Anomalies in electron density appeared about 40 days before the Maduo Mw7.3 earthquake, exhibiting an evolution process of “appearance-continuation-disappearance-reappearance-disappearance”. The IPI hotspot maps derived from descending (daytime) and ascending (nighttime) data showed similar trends.

The IPI method, with its high spatio-temporal resolution and adaptability to remove background trends and noise, can capture the spatio-temporal evolution of ionospheric parameters over and around earthquake areas, as well as potential strong seismic ionospheric anomaly signals. Such capabilities are instrumental in investigating the physical mechanisms behind the earthquake-ionosphere coupling

process. However, accurately identifying earthquake ionospheric precursors from electromagnetic satellite data remains a challenging task. Due to the complexity of earthquake preparation mechanisms, the discontinuity of observational data, and limitations in data analysis methods, numerous challenges persist, requiring a multidisciplinary approach to address them. Finally, it is important to acknowledge that the research on the IPI method is in its early stages, necessitating ongoing optimization of the method and statistical analysis of seismic instances.

Acknowledgement

We are grateful to Prof. Chen Chien-Chih of National Central University at Taiwan for providing the PI code, and to Prof. Wu Zhongliang, Zhang Xuemin, Liu Jing, and master's student Dong Lei of the Institute of Earthquake Prediction, China Earthquake Administration (IEPCA), for their help in constructing the idea of the thesis, data processing. CSES satellite data were obtained from (http://leos.ac.cn), F10.7 index and Kp index data were obtained from the German Center for Geoscientific Research (https://www.gfz-potsdam.de/), Dst index was obtained from the Geomagnetic Data Center of Kyoto University at Japan (https://wdc.kugi.kyoto-u.ac.jp/wdc/Sec3.html), and seismic catalogs were obtained from USGS (https://wdc.kugi.kyoto-u.ac.jp/wdc/Sec3.html). This work was funded by the National Key Research and Development Program of the Ministry of Science and Technology of China (2018YFE0109700), the National Natural Science Foundation of China(60214402) and the Joint Fund for Earthquake of the National Natural Science Foundation of China (U2039207). All figures were drawn using GMT (Wessel *et al*., 2019).

References

1.Chang X, Zou B, Guo J, et al. 2017. One sliding PCA method to detect ionospheric anomalies before strong Earthquakes: Cases study of Qinghai, Honshu, Hotan and Nepal earthquakes. *Advances in Space Research*, 59: 2058-2070.

2.Chen C, Rundle J, Holliday J, et al. 2005. The 1999 Chi-Chi, Taiwan, earthquake as a typical example of seismic activation and quiescence. *Geophysical Research Letters*, 32(22): L22315.

3.Dobrovolsky I, Zubkov S, Miachkin V. 1979. Estimation of the size of earthquake preparation zones. *Pure and Applied Geophysics*, 117: 1025-1044.

4.Dong L, Zhang X, Du X. 2022. Analysis of Ionospheric Perturbations Possibly Related to Yangbi *M*s6.4 and Maduo *M*s7.4 Earthquakes on 21 May 2021 in China Using GPS TEC and GIM TEC Data. *Atmosphere*, 13: 1725.

5.Du X, Zhang X. 2022. Ionospheric Disturbances Possibly Associated with Yangbi *M*s6.4 and Maduo *M*s7.4 Earthquakes in China from China Seismo Electromagnetic Satellite. *Atmosphere*, 13: 438.

6.Fejer B, Paula E, Gonzales S, et al. 1991. Average vertical and zonal F-region plasma drifts over Jicamarca. Journal of Geophysical Research Atmospheres, 96: 13901-13906.

7.Gokhberg M B, Morgounov V A, Yoshino T, et al. 1982. Experimental measurement of electromagnetic emissions possibly related to earthquakes in Japan. J. Geophys. Res, 87: 7824-7828.

8.Guo Y, Zhang X, Liu J, et al. 2022. Seismo-Ionospheric Effects Prior to Two Earthquakes in Taiwan Detected by the China Seismo-Electromagnetic Satellite. *Atmosphere*, 13(9): 1523.

9.Hayakawa M, Molchanov O A, Team N, et al. 2004. Summary report of NASDA's earthquake remote sensing frontier project. *Phys. Chem. Earth*, 29: 617–625.

10.Li M, Jiang X, Li J, et al. 2023. Temporal-spatial characteristics of Seismo-ionospheric influence observed by the CSES satellite. *Advances in Space Research*, doi: https://doi.org/10.1016/j.asr.2023.07.044.

11.Li M, Shen X, Parrot, M, et al. 2020. Primary joint statistical seismic influence on ionospheric parameters recorded by the CSES and DEMETER satellites, *Journal of Geophysical Research: Space Physics*, 125, e2020JA028116.

12.Li M, Wang H, Liu J, et al. 2022. Two Large Earthquakes Registered by the CSES Satellite during Its Earthquake Prediction Practice in China. *Atmosphere*, 13: 751.

13.Liu J, Zhang X, Yang X, et al. 2023. The Analysis of Lithosphere–Atmosphere–Ionosphere Coupling Associated with the 2022 Luding *M*s6.8 Earthquake. *Remote Sens*. 15: 4042.

14.Liu J, Guan Y, Zhang X, et al. 2021. The data comparison of electron density between CSES and DEMETER satellite, Swarm constellation and IRI model. *Earth and Space Science*, 8, e2020EA001475.

15.Liu J, Qiao X, Zhang X, et al. 2022. Using a Spatial Analysis Method to Study the Seismo-Ionospheric Disturbances of Electron Density Observed by China Seismo-Electromagnetic Satellite. *Front. Earth Sci*, 10: 811658.

16.Li X, Xu Y, An Z, et al. 2019. The high-energy particle package onboard CSES. *Radiation Detection Technology and Methods*, 3(3): 11.

17.Li Z, Yang B, Huang J, et al. 2022. Overview of space-based electric field data

584 processing methods. *Progress in Geophysics*, 1-15(In Chinese).

585 18.Marchetti D, Santis D, Shen X, et al. 2019. Possible
586 Lithosphere-Atmosphere-Ionosphere Coupling effects prior to the 2018 *M*w=7.5
587 Indonesia earthquake from seism, atmospheric and ionospheric data. *Journal of*
588 *Asian Earth Sciences*, 188: 104097.

589 19.Parrot M, Tramutoli V, Liu T, et al. 2021. Atmospheric and ionospheric coupling
590 phenomena associated with large earthquakes. *Eur. Phys. J. Spec. Top*, 230: 197–
591 225 2021.

592 20.Pulinets S, Ouzounov D. 2011. Lithosphere-Atmosphere-Ionosphere Coupling
593 （LAIC） model: An unified concept for earthquake precursors validation.
594 J*ournal of Asian Earth Sciences*, 41(4/5): 371-382.

595 21.Rikitake T. 1987. Earthquake precursors in Japan: precursor time and detectability.
596 *Tectonophysics*,136: 265–282.

597 22.Rundle J, Klein W, Tiampo K, et al. 2000. Linear pattern dynamics in nonlinear
598 threshold systems. *Physical Review E*, 61(3): 2418.

599 23.Rundle J, Tiampo K, Klein W, et al. 2002. Self-organization in leaky threshold
600 systems: The influence of near-mean field dynamics and its implications for
601 earthquakes, neurobiology, and forecasting. *Proceedings of the National*
602 *Academy of Sciences*, 99(suppl 1): 2514-2521.

603 Santis D, Marchetti D, Pavón-Carrasco F, et al. 2019. Precursory worldwide
604 signatures of earthquake occurrences on Swarm satellite data. *Sci Rep*, 9: 20287.

605 24.Santis D, Marchetti D, Perrone L, et al. 2021. Statistical Correlation Analysis of
606 Strong Earthquakes and Ionospheric Electron Density Anomalies as Observed by
607 CSES-01. *Il Nuovo Cimento C*, 44: 1–4.

608 25.Shen X, Yuan S, Zhima Z. 2023. Expanding Global Geophysical Field and Space
609 Environment Sensing Modeling Capabilities - The 5th Anniversary of ZH-1
610 Satellite in Orbit. *Space International*, 03: 31-37（in Chinese）.

611 26.Shen X, Zhang X, Yuan S, et al. 2018. The state-of-the-art of the China
612 Seismo-Electromagnetic Satellite mission. *Sci China Tech Sci*, 61: 634–642

613 27.SONDHIYA D, KUMAR S, GWAL A. 2014. On the possibility of precursors of
614 earthquakes in VLF range observed by DEMETER Satellite. *Nonlinear*
615 *Processes in Geophysics Discussions*, 1: 977-997.

616 28.Spogli L, Sabbagh D, Regi M, et al. 2021. Ionospheric response over Brazil to the
617 August 2018 geomagnetic storm as probed by CSES-01 and Swarm satellites and
618 by local ground-based observations, *Journal of Geophysical Research: Space*
619 *Physics*, 126, e2020JA028368.

620 29. Tiampo K, Rundle J, McGinnis S, et al. 2002. Eigenpatterns in southern California
621 seismicity, *J. Geophys. Res*, 107(B12): 2354.

622 30.Wessel P, Luis J, Uieda L, et al. 2019. The Generic Mapping Tools version
623 6. *Geochemistry, Geophysics, Geosystems*, 20: 5556–5564.

624 31.Wu A, Zhang Y, Zhou Y, et al. 2011. On the spatial-temporal characteristics of
625 ionospheric parameters before Wenchuan earthquake with the MPI method.
626 *Chinese Journal of Geophysics*, 54(10): 2445-2457(in Chinese).

627 32.Yan R, Parrot M, Pinçon J. 2017. Statistical study on variations of the ionospheric
628 ion density observed by DEMETER and related to seismic activities. *J. Geophys.*
629 *Res. Space Phys*, 122.

630 33.Yan R, Zhima Z, Xiong C, et al. 2020. Comparison of electron density and
631 temperature from the CSES satellite with other space-borne and ground-based
632 observations. *J. Geophys. Res. Space Phys*, 125, e2019JA027747.

633 34.Yao L, Zhang X, Yu T. 2014. A study of spacial correlation of monthly mean
634 deviation of ionospheric TEC over China. *Chinese Journal of Geophysics*, 57(11):
635 3600-3610 (in Chinese).

636 35.Yang C, Yong S, Wang X, et al. 2021. Research on Indonesia *M*s7.4 Earthquake
637 Based on Data of Zhangheng-1 Electromagnetic Satellite. *Acta Scientiarum*
638 *Naturalium Universitatis Pekinensis*, 57(06): 997-1005.

639 36.Yang Y, Hulot G, Vigneron P, et al. 2021. The CSES global geomagnetic field
640 model (CGGM): an IGRF-type global geomagnetic field model based on data
641 from the China Seismo-Electromagnetic Satellite, *Earth Planets Space*. 73: 45.

642 37.Zhang S, Zheng J, Jiang C, et al. 2017. Optimal analusis of parameter settings in
643 pattern informatics(PI) algorithm: An example of Shandong and adjacent areas.
644 *Chinese Journal of Geophysics*, 60(12): 4633-4643 (in Chinese).

645 38.Zhang X, Wang Y, Boudjada MY, et al. 2020 Multi-Experiment Observations of
646 Ionospheric Disturbances as Precursory Effects of the Indonesian *M*s6.9
647 Earthquake on August 05, 2018. *Remote Sensing*, 12(24): 4050.

648 39.Zhang Y, Li M, Huang Q, Shao Z, et al. 2023. Statistical correlation between
649 DEMETER satellite electronic perturbations and global earthquakes with $M \geq 4.8$.
650 *IEEE TRANSACTIONS ON GEOSCIENCE AND REMOTE SENSING*, 61: 1-18.

651 40.Zhang Y, Wang T, Chen W, et al. 2023. Are There One or More Geophysical
652 Coupling Mechanisms before Earthquakes? The Case Study of Lushan (China)
653 2013. *Remote Sensing*, 15: 1521.

654 41.Zhao S, Shen X, Li L, et al. 2021. A lithosphere-atmosphere-ionosphere coupling
655 model for ELF electromagnetic waves radiated from seismic sources and its
656 possibility observed by the CSES. *Science China(Technological Sciences)*, 64
657 (11): 2551-2559.

42.Zheng L, Yan R, Parrot M, et al. 2022. Statistical Research on Seismo-Ionospheric Ion Density Enhancements Observed via DEMETER. *Atmosphere*, 13: 1252.

43.Zhuo X, Zhao G, Wang J, et al. 2005. Seismo-Electromagnetic Satellite in Earthquake Prediction. *Journal of Geodesy and Geodynamics*, 02: 1-5.